Electronic Supplementary Material (ESI) for Energy & Environmental Science.
This journal is © The Royal Society of Chemistry 2017

Supplementary Materials

Direct Observation of Enhanced Water and Carbon Dioxide Reactivity on Multivalent Metal Oxides and Their Composites

Yi-Lin Huang[a], Christopher Pellegrinelli[a], Aaron Geller[b], Karen J. Gaskell[b] ,Sz-Chian Liou[c], Angelique Jarry[b], Luning Wang[b], Yi Yu[b], Hendrik Bluhm[d], Ethan J. Crumlin[d], Bryan W. Eichhorn[b], Eric D. Wachsman[a]

[a]University of Maryland Energy Research Center, University of Maryland, College Park, MD, 20742
[b]Department of Chemistry and Biochemistry, University of Maryland, College Park, MD, 20742
[c]AIMLab, Nano Center, University of Maryland, College Park, MD, 20742
[d]Advanced Light Source at Lawrence Berkeley National Laboratory, CA

Contents

Experimental section

Isotope exchange

Isotope saturated temperature programmed exchange (ISTPX) allows us to survey heteroexchange from the participation of lattice oxygen, and the interaction of multiple gases with the solid surfaces over a wide range of temperature and oxygen partial pressure (pO_2). Different types of isotope exchange techniques can be conducted either as a function of temperature, or isothermally at steady state to extract kinetic parameters. This study focuses on exploring the water and carbon dioxide reactivity on metal oxides in a wide range of temperature and pO_2; details of isothermal studies are discussed in depth in our previous work. *(45)*

The experiment set up of isotope exchange is shown in Fig. S1. $La_{0.6}Sr_{0.4}Co_{0.2}Fe_{0.8}O_{3-\delta}$ (Praxair) and $(La_{0.8}Sr_{0.2})_{0.95}MnO_{3\pm\delta}$ (LSM) (Fuel Cell Materials), $(Y_2O_3)_{0.08}(ZrO_2)_{0.092}$ (TOSOH), and $Ce_{0.90}Gd_{0.10}O_{1.95}$ (Fuel Cell Materials) powder were weighed out with a normalized surface area of 0.1 m^2. These materials were selected due to their widespread use in solid oxide fuel (and electrolysis) cell (SOFC/SOEC), and their inherently different material properties. For composites, LSM and YSZ, or LSCF and GDC, the powders were mixed and pretreated at 850°C in $p^{16}O_2$=0.05 atm for 30 minutes. The surface area, determined by BET, for LSCF, LSM, YSZ, GDC, LSCF-GDC, LSM-YSZ is 6.5, 5.6, 12.5, 11.1, 5.7 and 6.4 m^2/g, respectively. Sample powders were put in a quartz tube reactor with an inner diameter of 2mm. Multiple gas tanks, including different concentrations of oxygen and carbon dioxide (all balanced with helium) and helium, were connected together and mass flow controllors were used to provide desired concentrations of each gaseous species. The total flow rate was fixed at 20 SCCM.

Samples were pretreated in $P^{18}O_2$= 0.025 atm (Sigma-Aldrich; 95 atomic % ^{18}O) at 800°C for LSCF and at 850°C for LSM, GDC, and YSZ for 30 minutes to clean of any adsorbed species and exchange lattice oxygen to ^{18}O. 1000 ppm Ar tracer balanced with helium is used as a carrier gas to trace the flowing of $^{18}O_2$. After pretreatment, the reactor was air-cooled down to room temperature in 3 minutes. Then powder samples were held under helium flow for 30 minutes to clean up any weakly bonded absorbents and then switched to the desired gas compositions and oxygen partial pressure. Due to the overlapping m/z signal of H_2O and ^{18}O (m/z=18) in mass spectrometer, D_2O (m/z=20) was used to identify the exchange of water with the surface. When the signals of all gases reach steady state, the temperature was raised up at a fixed ramp rate (30°C/min) under a given gas compositions and the evolution of oxygen-containing isotopologues, including $D_2{}^{16}O$, $D_2{}^{18}O$, $^{16}O_2$, $^{16}O^{18}O$, $^{18}O_2$, $C^{16}O_2$, $C^{16}O^{18}O$, and $C^{18}O_2$, were recorded using quadrupole mass spectrometer (QMS). The isotope exchange results were then summarized in temperature-PO_2 domain to visualize water and CO_2 exchange on the solid surfaces.

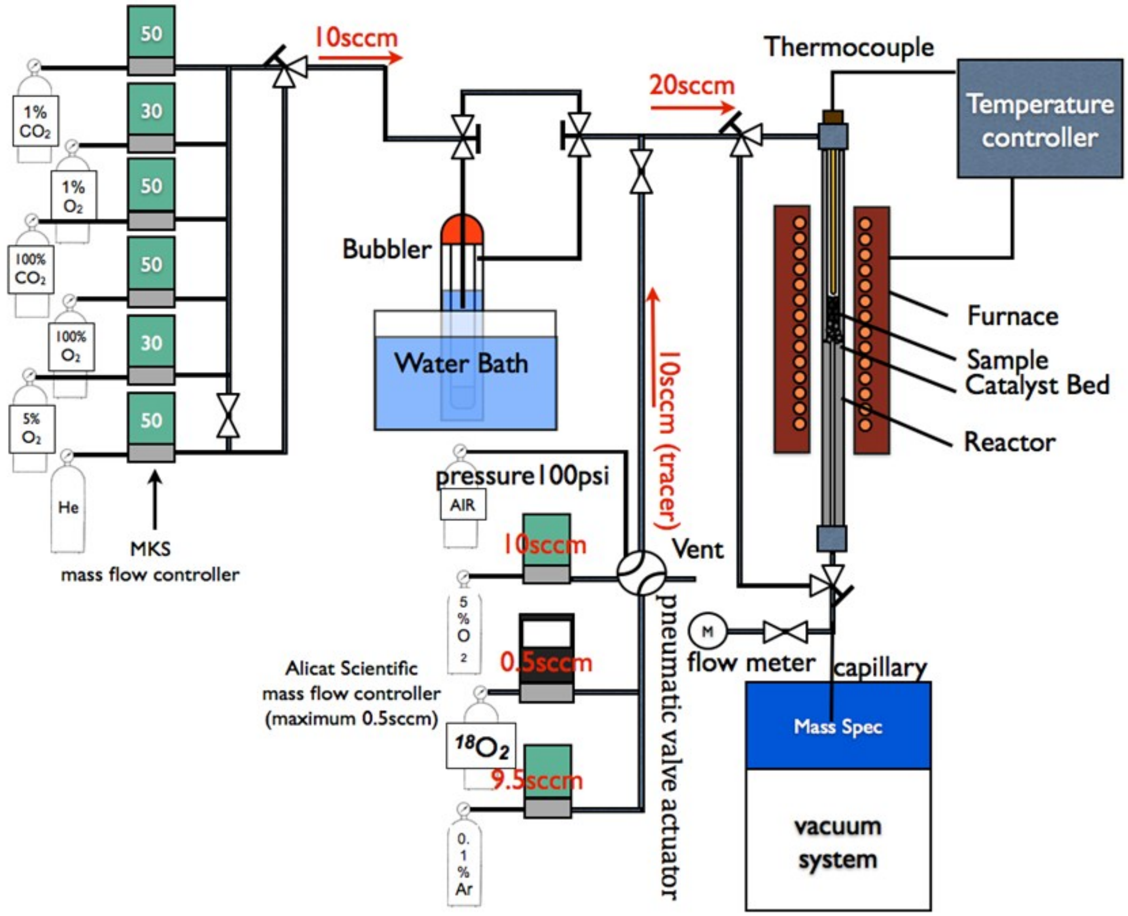

Fig. S1 Experimental set-up of oxygen isotope exchange consists of four major parts: 1). Gasses sources, 2) oxygen isotope gas stream, 3) a temperature controlled quartz reactor, and 4) an Extrel quadrupole mass spectrometer (QMS),

To quantitatively determine gas concentration, the QMS was calibrated before and after experiment by flowing different concentrations of CO_2 and O_2 (AIRGAS). D_2O concentration was calibrated by flowing different amounts of gas through a quartz frit impringer with a balanced bypass gas to establish a total fixed flow rate of 20SCCM. The temperature of the water bath was controlled by a thermoelectric cooling system with a deviation of +/- 0.2°C throughout each experiment. D_2O vapor pressure was determined using temperature readings and a temperature/vapor pressure database provided by NIST. The use of heavy water enables us to calibrate the concentrations of water isotopologues much accurately.

in situ APXPS

- Sample Preparation

LSM and LSM-YSZ (1:1 weight ratio) pads were dropcoated onto a single-side polished YSZ (8 % mol Y_2O_3) single crystal with 111-orientation (*MTI Corporation*). The sample was heated to an intermediate temperature of 400^{o}C with a 1 hour dwell time before heating to 1200^{o}C for 2 hours in air. Both heating and cooling rates were 2^{o}C/min.

- Sample Set-up

APXPS experiments were performed at the Advanced Light Source (ALS) at the Lawrence Berkeley National Laboratory. Two beamlines, 9.3.2 and 11.0.2, were utilized for different experiments. Five different gas environments were used in the experiments:

Environment	**Pressure (mTorr)**
O_2	200
H_2O	50
$O_2 + H_2O$	200 and 50 respectively
CO_2	200
$O_2 + CO_2$	200 and 200 respectively

The sample was oriented so that the X-ray beam struck the sample at incident angle of 75^{o} and the electron emission angle was 0^{o} with respect to the sample normal. Mn 3s spectra were collected at photon energies of 490 eV, and were analyzed with the CasaXPS program.

The difference in the ^{18}O source

Gas-solid oxygen exchange consists of multiple, sequential reactions and is often limited by a single rate-limiting step. The first step is adsorption, where gaseous molecules form surface intermediate species, bonding (chemically) to an available surface site. The next reaction step is dissociation, where the oxygen bond (with O, C, or H) is broken, followed by transport of dissociated oxygen atoms into nearby lattice sites. The final step is the ion incorporation, in which the presence of surface vacancies is necessary. Oxygen exchange proceeds as a series of these three basic steps.

The design of ISTPX focuses on the investigation of gas-solid exchange process. In ISTPX, lattice ^{18}O is the source of ^{18}O. By tracking of the movement of labeled ^{18}O, ISTPX provides a molecular point of view of how gaseous molecules exchange with lattice oxygen.

In isotope temperature programmed exchange (TPX), $^{18}O_2$ is the source of labeled oxygen. Because labeled ^{18}O is in gas phase rather than solid phase, TPX can survey the temperature region where homoexchange occurs. An example of the difference between ISTPX and TPX of YSZ is shown in Fig. S2. In TPX, as shown in Fig. S2 (A) and (B), the formation of labeled $D_2{}^{18}O$ requires both the dissociation of $^{18}O_2$ and D_2O on YSZ. The observed exchange from TPX provides a direct probe of homogeneous gas-gas exchange process on the YSZ surface, but is only observed at greater than 600°C. In contrast, ITSPX allows us to probe the interaction between D_2O and the YSZ surface before the dissociation of O_2 occurs. As shown in Fig. S2 (C) and (D), water exchange around 150°C while O_2 exchange is above 650°C. Therefore, the gas-solid exchange between water and the YSZ surface can be observed.

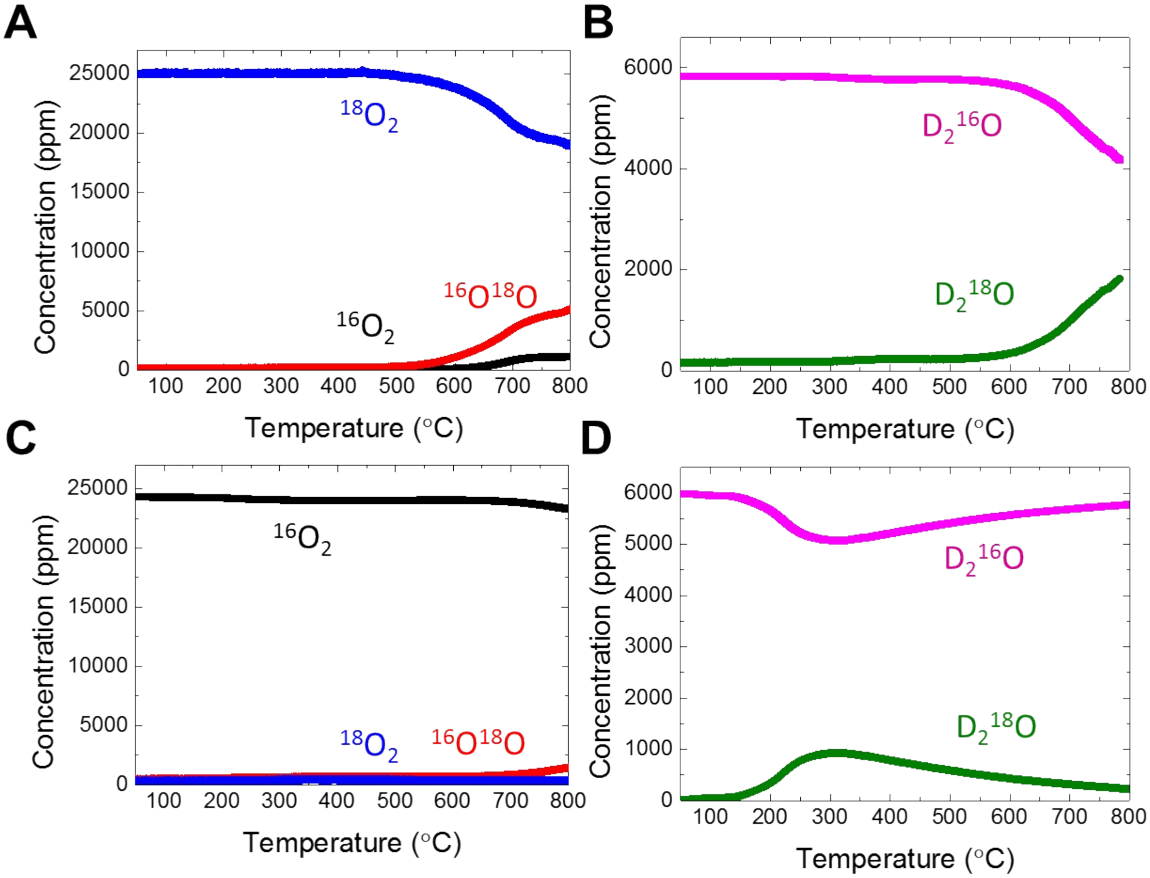

Fig. S2. (A) O_2 and (B) D_2O signal of TPX with the presence of 25000ppm $^{18}O_2$ and 6000ppm D-$_2$O. (C) O_2 and (B) D_2O signal of ISTPX with the presence of 25000ppm $^{16}O_2$ and 6000ppm D_2O.

ISTPX of LSM and LSM-YSZ with the Presence of Gaseous Oxygen-Containing Species

ISTPX of LSM and LSM-YSZ composite in the presence of both 25000ppm $^{16}O_2$ and 6000ppmm D_2O is shown in Fig. S3. The oxygen signal, Fig. S3 (A), shows that O_2 exchange on LSM only happens above 650°C. The onset temperature of O_2 exchange on LSM-YSZ composite is around 400°C and a separate exchange peak can be observed above 650°C. Fig. S3

(B) shows the D_2O signal of LSM and LSM-YSZ composite. The onset temperature of D_2O exchange on composite is about 150°C while LSM only exchanges its own lattice oxygen with water above 650°C. O_2 and CO_2 signal of ISTPX of LSM and LSM-YSZ composite with the presence of both 25000ppm O_2 and 2500ppmm CO_2 is shown in Fig. S4 (A) and (B), respectively. The onset temperature of CO_2 exchange on LSM-YSZ is about 150°C while the onset temperature of CO_2 exchange on LSM is about 650°C.

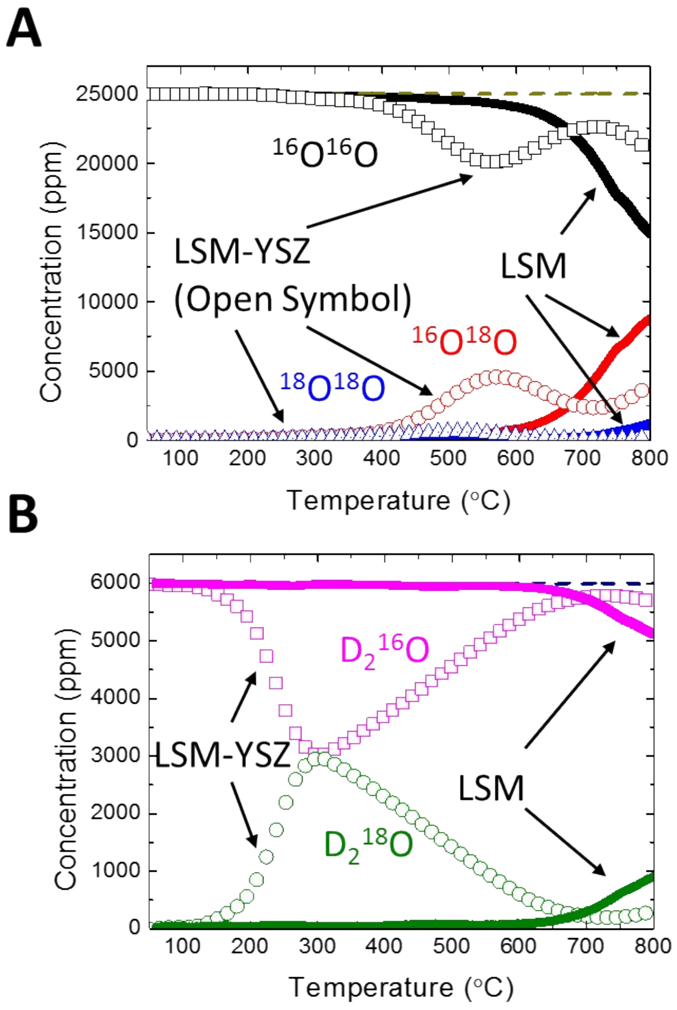

Fig. S3 (A) O_2 signals and (B) D_2O signals for ISTPX of LSM (solid symbol) and LSM-YSZ(open symbol) with the presence of both O_2 (25000ppm) and D_2O (6000ppm).

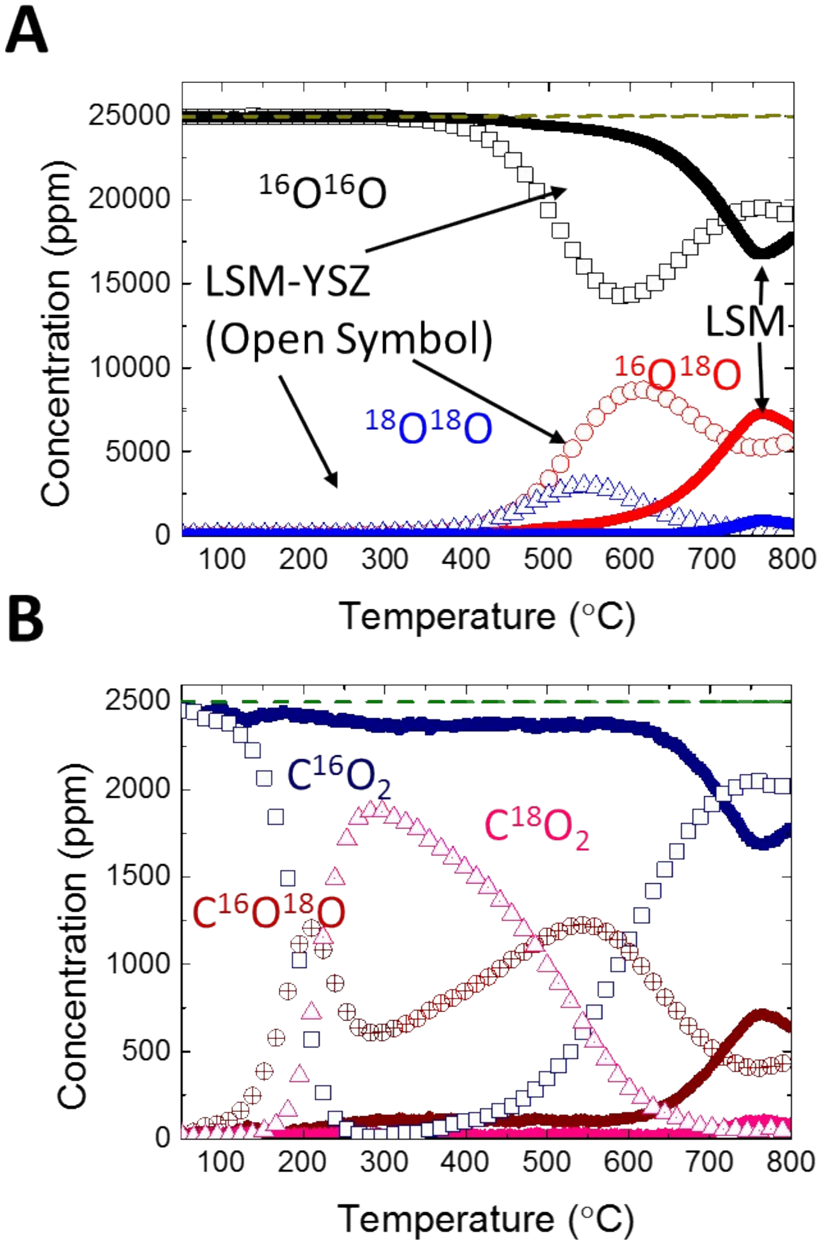

Fig. S4. (A) O_2 signals and (B) CO_2 signals for ISTPX of LSM (solid symbol) and LSM-YSZ(open symbol) with the presence of both O_2 (25000ppm) and CO_2 (2500ppm).

The number of lattice oxygen sites is calculated based on the theoretical density of each material, and the known sample weight. Using this and the amount of ^{18}O that is exchanged to the gas phase, we can infer that not only surface oxygen, but also lattice oxygen, participates in the exchange reaction. *(32)*

Construction of contour plots for water and CO_2 exchange rate

Temperature and PO_2 can affect the surface configurations of multivalent metal oxides dramatically by altering the interactions between the catalyst surface and oxygen-containing species. ISTPX spectra demonstrate the effects of temperature on exchange rate of water or CO_2 at a specific PO_2. Using multiple ISTPX spectra at different PO_2's, we can construct a 3D diagram for exchange versus temperature and PO_2. Fig. S5 shows the process of constructing a 3D diagram for water exchange of LSM-YSZ. Each ISTPX spectra represents just one of many slides on the 3D diagram. The contour plot is the projection of the 3D exchange diagram. The use of a contour plot helps to visualize the water and CO_2 exchange rate as a function of temperature and PO_2.

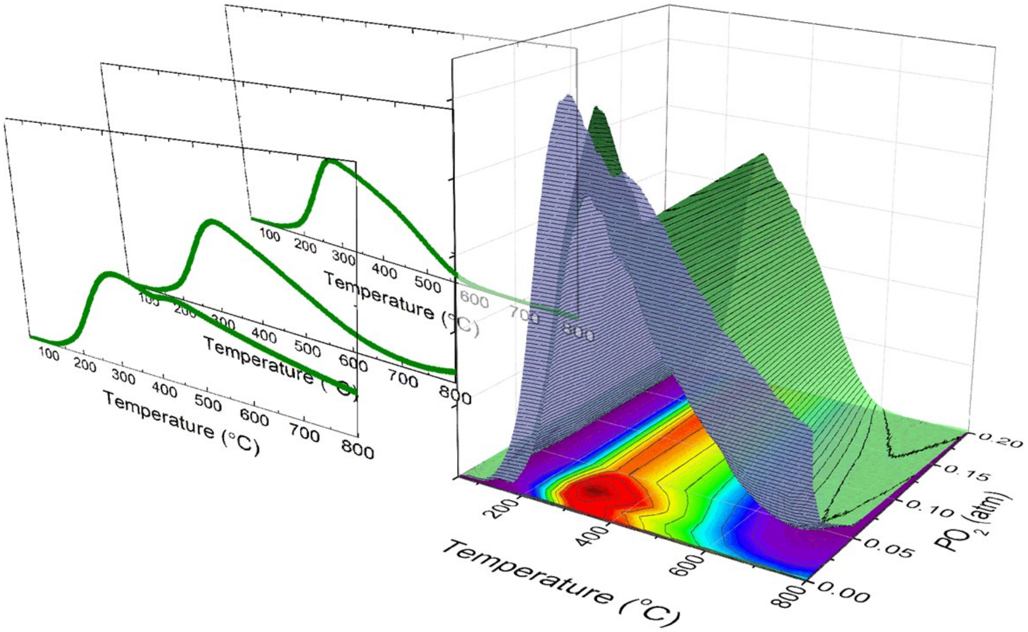

Fig. S5. An example of building a contour plot for the exchange of water on LSM-YSZ based on ISTPX results for multiple PO_2's. A 3D water exchange diagram, where x axis is temperature, y axis is PO_2 and z axis is concentration of water being exchanged to isotopically labeled $D_2{}^{18}O$, can be constructed and each slide represents one ISTPX spectra at a specific PO_2.

Singly and Doubly exchanged CO_2 on the solid surfaces

Due to the diatomic nature of CO_2, CO_2 exchange can be distinguished into singly exchanged CO_2 ($C^{16}O^{18}O$) and doubly exchanged $C^{18}O_2$ based on the numbers of oxygen in CO_2 participating in the exchange. The single exchange CO_2 can occur through the formation of carbonate (CO_3) on the surface and exchange one of its oxygen with lattice oxygen. The double exchange could occur though bidentate carbonate migration: two exchange with a swing during one absorption. It is difficult to determine whether singly and doubly exchanged CO_2 is caused by multiple back exchange or a different exchange mechanism.

Contour plots of singly, doubly, and total exchanged CO_2 on GDC are shown in Fig. S6 (D-F) and on LSCF-GDC composite are shown in Fig. S6 (G-I). CO_2 begins to exchange with YSZ above 150°C and double heteroexchange dominates above 250°C. Above 250°C, CO_2 starts to exchange with LSCF though single heteroexchange, and at higher temperature, above 350°C, double heteroexchange dominates. The presence of dual phase in LSCF-GDC composite does not enhance any CO_2 exchange level in single or double CO_2 exchange signals.

Contour plots of singly, doubly, and total exchanged CO_2 exchange on LSM, YSZ, and LSM-YSZ are shown in Fig. S7. CO_2 exchange on LSM-YSZ composite is normalized to the YSZ surface area, due to a lack of exchange with LSM, to emphasize the effect of the composite material. Both singly and doubly exchanged LSM-YSZ shows an enhancement in the exchange level, compared with LSM and YSZ separately.

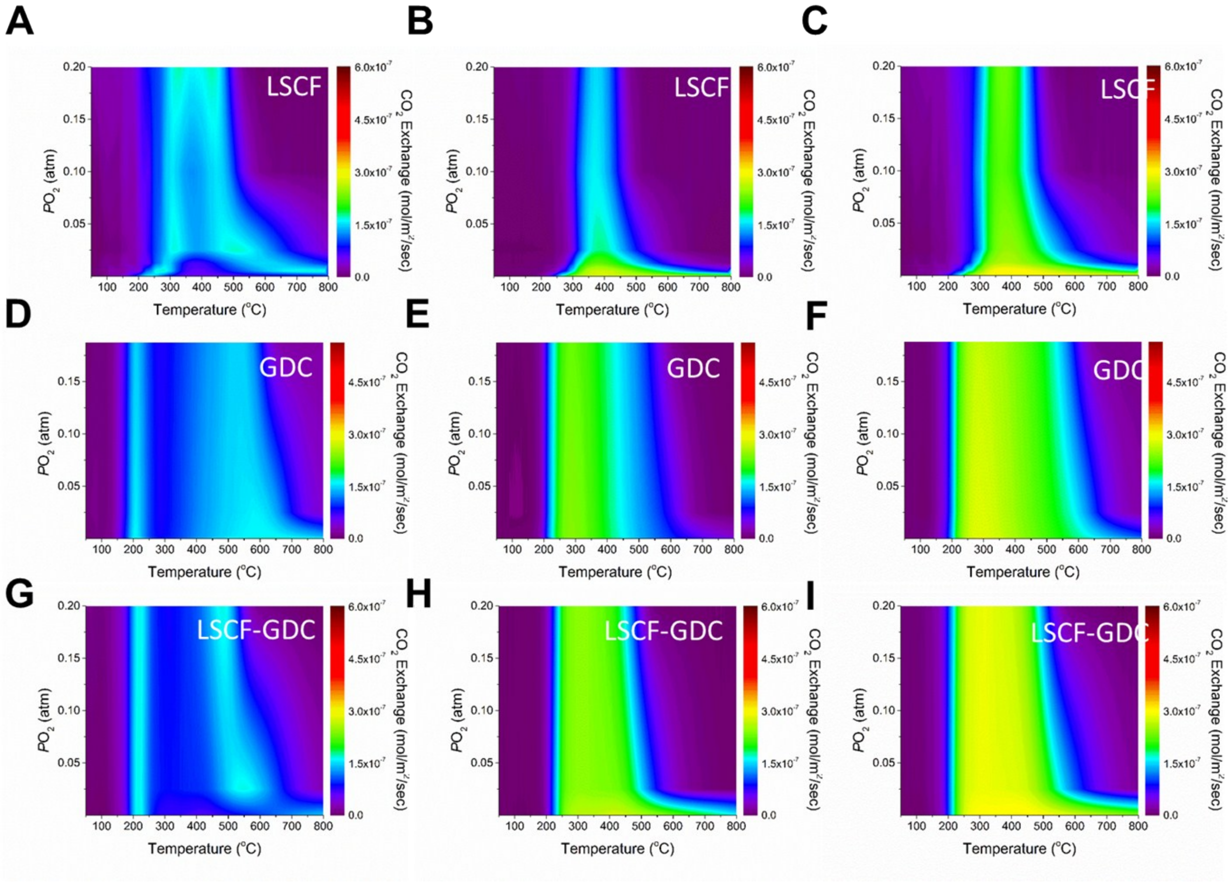

Fig. S6. Contour plots of CO_2 isotope exchange as a function of temperature and PO_2 on LSCF with (a) single, (b) double, and (c) total heteroexchange, on GDC with (d) single, (e) double, and (f) total heteroexchange, and on LSCF-GDC composite with (g) single, (h) double, and (i) total heteroexchange.

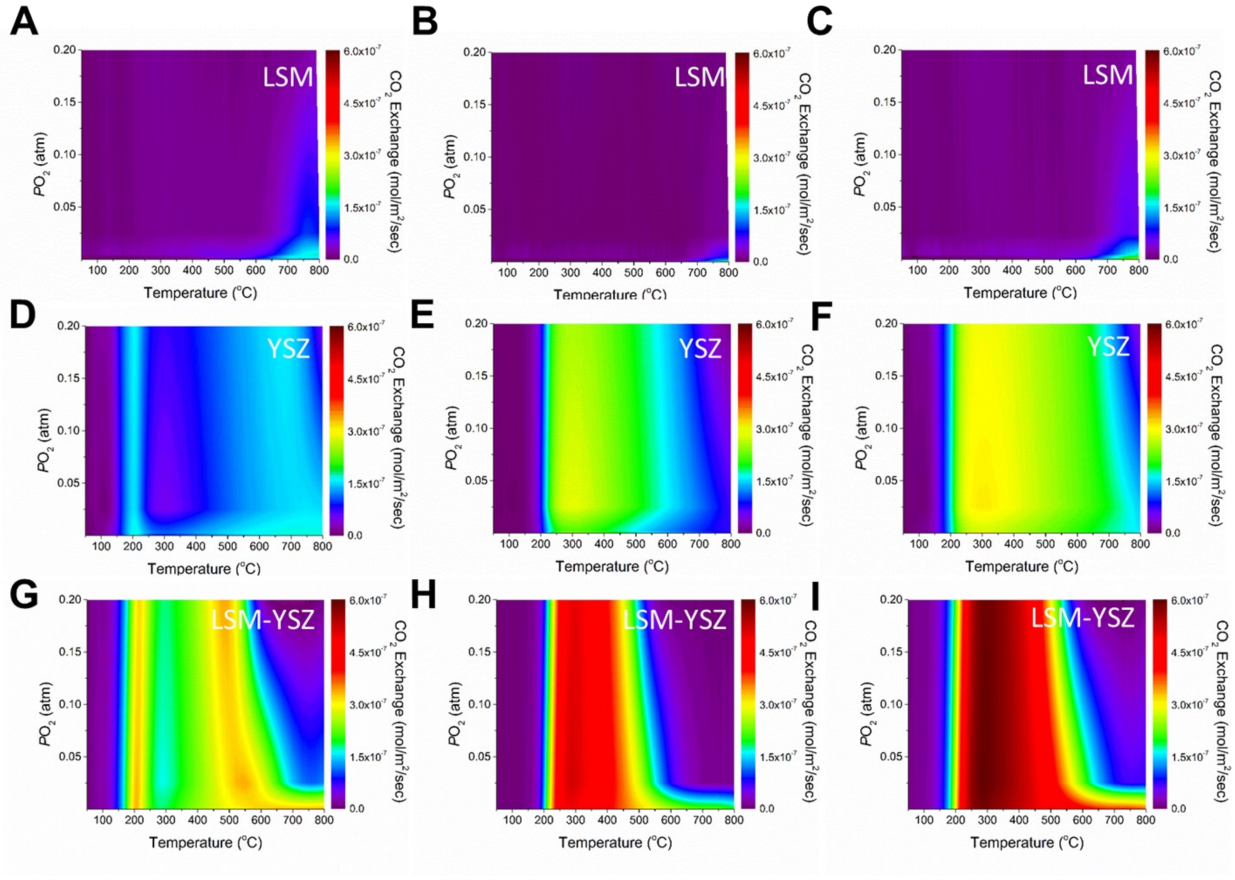

Fig. S7. Contour plots of CO_2 isotope exchange as a function of temperature and PO_2 on LSM with (a) single, (b) double, and (c) total heteroexchange, on YSZ with (d) single, (e) double, and (f) total heteroexchange, and on LSM-YSZ composite with (g) single, (h) double, and (i) total heteroexchange.

Mn 3s Spectra and Mn Redox State Determination

Mn 3s spectra were taken to evaluate the Mn redox state in LSM and LSM-YSZ materials. It is well established that the Mn 3s spectrum exhibits two peaks from spin-spin coupling and that a greater difference in energy (ΔE) between the two peaks is indicative of more reduced Mn. A linear relationship between redox state and ΔE can be determined: *(46-50)*

$$Mn\ Redox\ State = \frac{-(\Delta E - 8)}{0.9} \qquad (1)$$

For peak fitting, a Shirley background was used and peaks were fit with a Gaussian Lorentzian mix of 70:30.

Auxiliary XPS results

Due to the difficulty in accurately measuring Mn 3 S signals under ambient pressure conditions, replicating experiments have been carried out in the same beamline and *ex situ*. We conducted similar *in situ* XPS studies on these materials in another experiment and addition *ex situ* XPS studies and observed similar results, as shown in Fig. S8. It is also worth noting that in the *ex situ* studies, the full width half maximum (FWHM) is nearly the same in both materials, while in the *in situ* studies (Fig. 4 and Fig. S8), the LSM shows a broader FWHM. One possible explanation for this is that *in situ,* there is a lower concentration of Mn at the surface relative to the bulk of the composite material compared to in the pure LSM. This would imply a lower concentration of under-coordinated surface Mn in the composite material compared to the pure LSM, and thus the composite would have a narrower FWHM (signifying a lower variability in coordination environments).

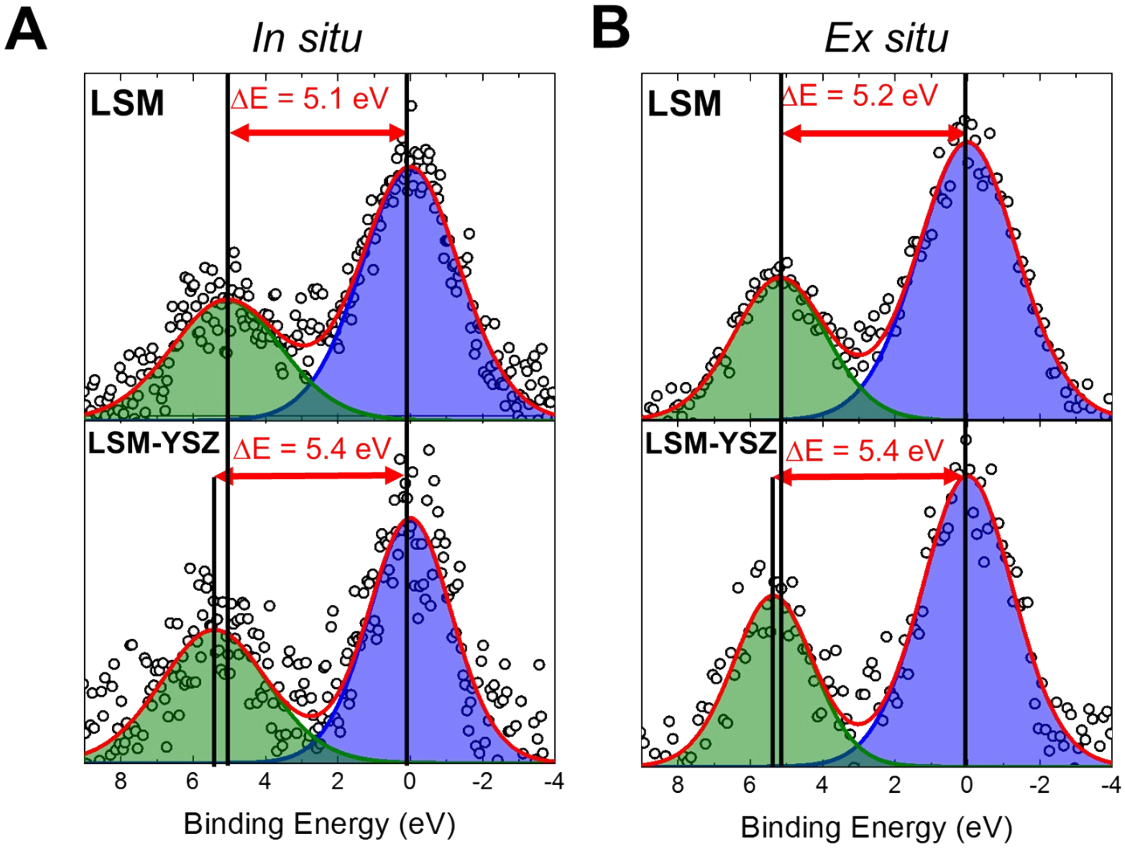

Fig. S8. XPS replicating experiments. XPS spectra of LSM and LSM-YSZ composite carried out (A) in the same beamline as Fig. 4 and (B) *ex situ*.

TEM and EELS Analysis on LSM-YSZ Composite

Transmission electron microscopy (TEM) and electron energy loss spectroscopy (EELS) analysis was conducted on LSM-YSZ composite, as shown in Fig. S9. LSM-YSZ powder was pretreated at 800°C for 30 minutes in PO_2=0.025atm. Energy-dispersive X-ray spectroscopy (EDX) elemental mapping is shown in Fig. S9 (A), where LSM particles are identified through the overlapping of La, Sr and Mn signals. A TEM image of the LSM-YSZ interface is shown in Fig. S9 (B). There are no detectable secondary phases. According to elemental mapping through EELS at the interface shown in Fig. S9 (C), no inter-diffusion between LSM and YSZ is observed. Fig. S9 (D) shows EELS spectra for the O $\boldsymbol{K}$ edge and Mn $\boldsymbol{L_{2,3}}$ edge on YSZ, LSM, and at the interface. The changes of O ***K*** edge (loss of the peak at ~530 eV) suggest that a higher concentration of oxygen vacancy at the interface. The EELS spectra as s function of distance from the interface is shown in the contour plot in Fig. S9 (E), where the x-axis is binding energy and y-axis is the distance from the interface. The color map represents the intensity of peaks. EELS spectra of Mn $\boldsymbol{L}_{2,3}$ edge as a function of distance from the interface is shown in Fig. S9 (F). The spatial change of Mn oxidation state as a function of distance from the interface is calculated based on the intensity ratio of Mn (L_3/L_2) peaks.*(39, 40)* The results suggest that the Mn oxidation state is a mixture of 3+ and 4+ states on LSM, while Mn is reduced at the LSM-YSZ interface.

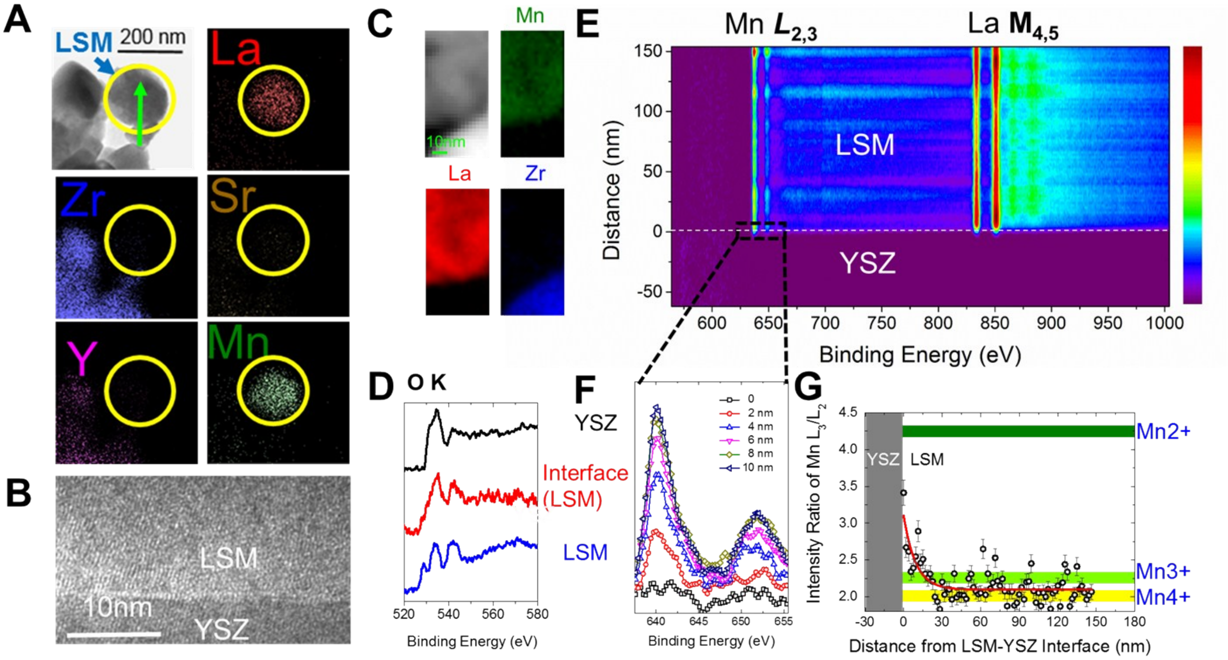

Fig. S9. TEM and EELS analysis on LSM-YSZ composite. (A) EDX elemental mapping of LSM-YSZ composite. LSM particle is highlighted in yellow circle. (B) HRTEM image on LSM-YSZ interface. (C) EELS elemental mapping of La, Mn, and Zr at the LSM-YSZ interface. (D) EELS spectra of O ***K*** edge on YSZ, LSM-YSZ interface (close to LSM side), and LSM. (E) Contour plot of EELS line-scan spectra across the LSM-YSZ interface, as shown on the green line in (A), shows the spectral feature changes of Mn $\boldsymbol{L}_{2,3}$ edge and La $\boldsymbol{M}_{4,5}$ edge. (F) Enlarged spectra of Mn $\boldsymbol{L}_{2,3}$ edge signals at the interface with a step size of 2nm from the interface. (G)

Based on the intensity ratio of Mn L_3/L_2, Mn oxidation state as a function of distance from the interface is calculated.

Based on the results, the reduced Mn in LSM is catalytically active and the generation of oxygen vacancies can help the incorporation of oxygen into YSZ. The possible mechanism is proposed regarding the changes in defect chemistry at the LSM-YSZ interface. At the LSM-YSZ interface, the difference in oxygen chemical potential in LSM and YSZ bulk could lead to the generation of oxygen vacancies at the interface. Fig. S10 shows the oxygen vacancy concentration as a function of distance from the interface. These oxygen vacancies can be compensated by the reduction of Mn, for example, from 3+ to 2+ (or 4+ to 3+) due to charge balance:

$$2Mn_{Mn}^{x} + O_O{}^{x} \rightarrow 2Mn_{Mn}^{'} + V_O{}^{\circ\circ} + 1/2O_2 \qquad (3)$$

where $V_O{}^{\circ\circ}$ represents an oxygen vacancy with two positive charges. $Mn_{Mn}{}^{x}$ represents Mn occupies in Mn site with a neutral charge and $Mn_{Mn}{}^{'}$ is a reduced Mn in Mn site. In this case, the generation of oxygen vacancy may promote both the heteroexchange on LSM and interphase diffusion between LSM-YSZ, leading to the increase of water and CO_2 exchange rate on LSM-YSZ.

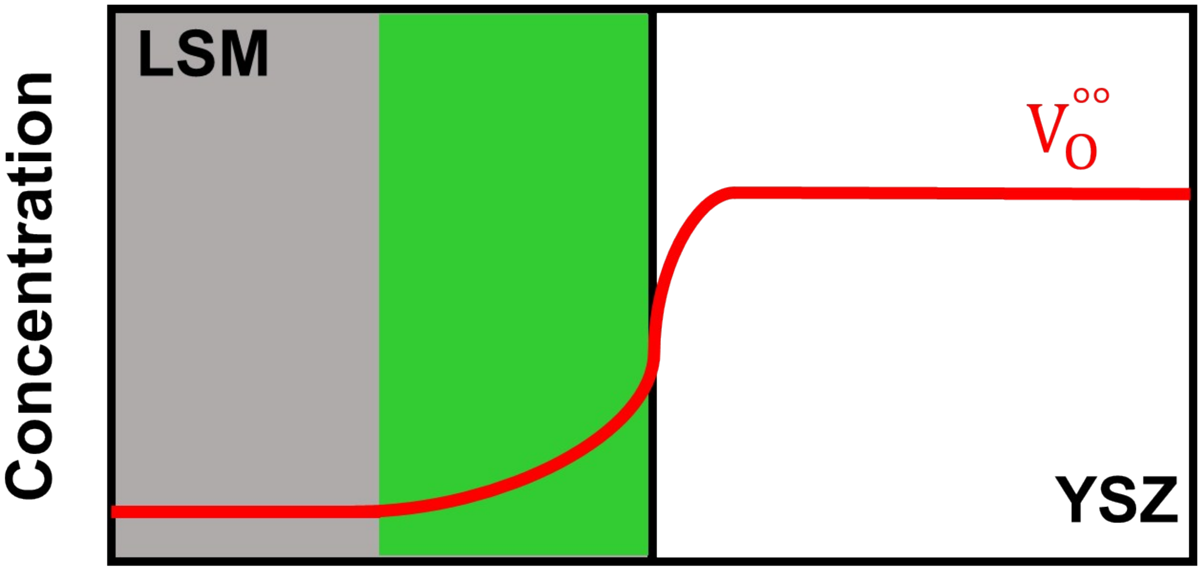

Fig. S10. The possible mechanism for the reduction of Mn in LSM-YSZ. The generation of oxygen vacancies to compensate the charge balance.

References

39. Z. Wang, J. Yin and Y. Jiang, *Micron*, 2000, **31**, 571-580.
40. M. Backhaus-Ricoult, *Solid State Ionics*, 2006, **177**, 2195-2200.
45. Y. L. Huang, C. Pellegrinelli and E. D. Wachsman, *Angew. Chem. Int. Ed.*, 2016, 55(49):15268-15271.
46. V. Galakhov, M. Demeter, S. Bartkowski, M. Neumann, N. Ovechkina, E. Kurmaev, N. Lobachevskaya, Y. M. Mukovskii, J. Mitchell and D. Ederer, *Physical Review B*, 2002, **65**, 113102.
47. M. Demeter, M. Neumann, V. Galakhov, N. Ovechkina, E. Kurmaev and N. Labachevskaya, *Acta Physica Polonica. Series A*, 2000, **98**, 587-591.
48. D. Shirley, *Phys. Scr.*, 1975, **11**, 117.
49. S.-J. Shih, R. Sharghi-Moshtaghin, M. R. De Guire, R. Goettler, Z. Xing, Z. Liu and A. H. Heuer, *J. Electrochem. Soc.*, 2011, **158**, B1276-B1280.
50. V. Brabers, F. Van Setten and P. Knapen, *J. Solid State Chem.*, 1983, **49**, 93-98.